Capacitively-Shunted Four Josephson Junctions Flux Qubit

Barkay GUTTEL

A report following the final internship
required for Master of Science

PhITEM
Université Grenoble Alpes
France

June 9, 2020

Contents

1 Introduction

In his canonical talk from 1981, Richard Feynman [1] laid the first stone towards quantum simulation and quantum computation. Since then, many physical realizations of the fundamental building block for quantum computers have been proposed, each claiming to be a potential candidate to become a useful quantum bit, or *qubit*. Out of these candidates, one promising category is the superconducting qubit.
Superconducting circuits show quantum properties despite their macroscopic size, are well- and fast-controllable and are scalable thanks to modern techniques and technology. There are three archetypes of superconducting qubits- charge, phase, and *flux qubits*, named after a main quantization phenomenon they show. Out of these the flux qubit, first proposed by Mooij, Orlando *et al.* in 1999 [2, 3], is a promising candidate [4] for *quantum annealing*, due to the double-well potential energy landscape, making even its ground state naturally represented as the superposition of two states.

Quantum annealing [5] is a process for finding a global minimum of a given function (implemented as a Hamiltonian), by adiabatically changing the effective Hamiltonian from the start Hamiltonian, whose ground state is known and can be easily achieved, to the final one, which corresponds to the target function. In general, the system should stay at the (instantaneous) ground state during the entire process, and the adiabatic theorem [6] guarantees it under some conditions. Realizing a useful quantum annealer can greatly help in combinatorial optimization problems, both scientific [7] and day-life [8].

While the objective of a universal quantum computer can achieve unprecedented accomplishments, and is actively pursued by many groups, an alternative pursuit with shorter-term goals is of the essence. In his summary of the current Noisy Intermediate-Scale Quantum (NISQ) era, John Preskill concluded: "Since theorists have not settled whether quantum annealing is powerful, further experiments are needed" [9]. This bat-signal [10] will be answered.

2 Capacitively-Shunted Flux Qubit

Several improvements and modifications have been proposed over the years to the first design of the flux qubit, consists of three Josephson junctions interrupting a wire loop, with one junction smaller than the others. In 2007, You *et al.* [11] suggested that the adding of a shunt capacitor in parallel with the small Josephson junction would decrease its sensitivity to charge noise. In addition, this will allow the small junction to be smaller and thus decrease flux noise as well. This report concerns with the design of this type of qubits, only with four Josephson junctions, instead of the original three. This addition is due to the fact that shadow evaporation [12], the most commonly used technique for fabrication of Josephson junctions, inherently creates an even number of junctions [13]. Fabrication of three Josephson junctions devices with this technique is still common, and the fourth junction is assumed to have much larger area, and so negligible effect. Here, however, we chose to explicitly include it in the design, albeit added complexity. Therefore from now on the flux qubit considered is the capacitively-shunted four Josephson junctions (CS4JJ) qubit.

2.1 Mathematical Derivation of the Hamiltonian

In this section, we will derive the CS4JJ qubit Hamiltonian in its most general form, i.e. shunting capacitances on four Josephson junction, in addition to their intrinsic capacitances, and with possibly different junction areas. In practice, however, the design we were working on only includes shunting capacitance over the small ($\alpha-$) junction while the other three are of the same area, see Fig 1.
Two circuit diagrams are shown, for floating and grounded CS4JJ qubits. For the Hamiltonian derivation we use the floating qubit notation (Fig 1a) but this Hamiltonian describes both designs, up to small modifications.

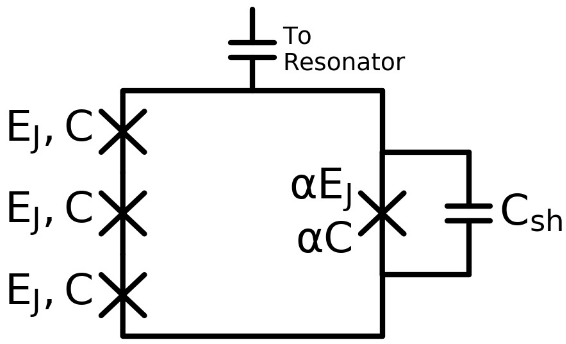

(a)

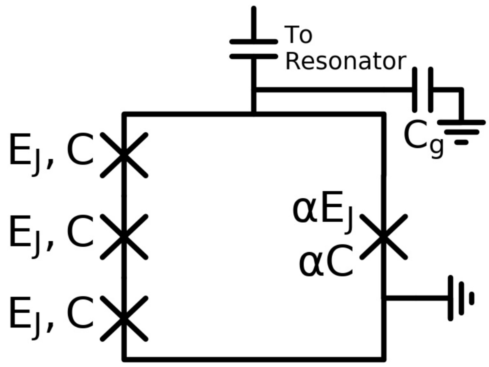

(b)

Figure 1: Schematic circuit diagrams of (a) floating and (b) grounded capacitively-shunted four Josephson junctions (CS4JJ) qubit. Notice that by considering a wire between the two connections (direct and capacitive) to the ground plane, the two circuits are equivalent up to $C_{sh} \leftrightarrow C_g$. Other capacitances (e.g. between floating qubit and ground plane) are omitted for simplicity.

2.1.1 Classical Calculation

The four-junction-qubit is made of three identical Josephson junctions, up to a small deviation, with area ratios β_i and hence Josephson energy $E_{Ji} = \beta_i E_J$, intrinsic capacitance $C_i = \beta_i C$, with $i = \{1, 2, 3\}$. It is possible to also add shunting capacitance $C_{sh} = \lambda C$ over these junctions. The fourth Josephson junction is smaller by ratio α and therefore has Josephson energy $E_{J4} = \alpha E_J$ and intrinsic capacitance $C_i = \alpha C$. In the capacitively-shunted design a shunt capacitor is added in parallel, and we denote the shunting capacitance $C_{sh} = \zeta C$.
In order to find the capacitive energy of a junction, $CV^2/2$, we use the Josephson relation [14] for the voltage drop across junction i, $V_i = (\Phi_0/2\pi)\dot{\varphi}_i$, where $\Phi_0 = h/2e$ is the magnetic flux quantum

and φ_i is the phase difference over the ith junction. We will also use the quantization condition of the total phase in the loop $\sum_i \varphi_i + 2\pi(\Phi_{ext}/\Phi_0) = 2\pi n,\ n \in \mathbb{N}$, where Φ_{ext} is the external magnetic flux.

In the following, we find the Hamiltonian of the qubit's following techniques from the field of circuit quantum electrodynamics [15], see Sec. 4.
First we use the relations above to get the total capacitive energy for the Josephson junctions

$$T(\vec{\varphi}) = \frac{C}{2}\left(\frac{\Phi_0}{2\pi}\right)^2 \left[(\beta_1+\lambda)\dot{\varphi}_1^2 + (\beta_2+\lambda)\dot{\varphi}_2^2 + (\beta_3+\lambda)\dot{\varphi}_3^2 + (\alpha+\zeta)\left(\dot{\varphi}_1+\dot{\varphi}_2+\dot{\varphi}_3\right)^2\right]. \tag{1}$$

The Josephson energy of a junction is $U(\varphi_i) = E_{Ji}(1-\cos(\varphi_i))$, where $E_J = (\Phi_0/2\pi)I_c$ with I_c the critical current of the junction (this current depends on the junction area and the insulation thickness between superconductors). Using the same quantization condition and dropping the constants we get the total Josephson energy,

$$U(\vec{\varphi}) = -E_J\left[\beta_1\cos(\varphi_1) + \beta_2\cos(\varphi_2) + \beta_3\cos(\varphi_3) + \alpha\cos\left(\varphi_1+\varphi_2+\varphi_3+2\pi\frac{\Phi_{ext}}{\Phi_0}\right)\right]. \tag{2}$$

The conjugate variables of the Lagrangian $\mathcal{L} = T\left(\dot{\vec{\varphi}}\right) - U(\vec{\varphi})$ are

$$\begin{pmatrix} q_1 \\ q_2 \\ q_3 \end{pmatrix} = \begin{pmatrix} \dfrac{\partial\mathcal{L}}{\partial\dot{\varphi}_1} \\ \dfrac{\partial\mathcal{L}}{\partial\dot{\varphi}_2} \\ \dfrac{\partial\mathcal{L}}{\partial\dot{\varphi}_3} \end{pmatrix} = C\left(\frac{\Phi_0}{2\pi}\right)^2 \begin{pmatrix} a+b_1 & a & a \\ a & a+b_2 & a \\ a & a & a+b_3 \end{pmatrix} \begin{pmatrix} \dot{\varphi}_1 \\ \dot{\varphi}_2 \\ \dot{\varphi}_3 \end{pmatrix} = \mathbf{M}\begin{pmatrix} \dot{\varphi}_1 \\ \dot{\varphi}_2 \\ \dot{\varphi}_3 \end{pmatrix} \tag{3}$$

where we made the change of variable $b_i \equiv \beta_i + \lambda$ and $a \equiv \alpha + \zeta$.
The capacitive part of the Hamiltonian is then

$$\sum_i q_i\dot{\varphi}_i - T\left(\dot{\vec{\varphi}}\right) = \frac{1}{2}\dot{\vec{\varphi}}\cdot\mathbf{M}\dot{\vec{\varphi}}. \tag{4}$$

The inverse relations can be calculated by the inverse matrix. We write them explicitly for completeness:

$$\dot{\varphi}_1 = \frac{1}{C\left(\frac{\Phi_0}{2\pi}\right)^2}\left[\frac{\{a(b_2+b_3)+b_2b_3\}\,q_1 - ab_3q_2 - ab_2q_3}{a(b_1b_2+b_2b_3+b_3b_1)+b_1b_2b_3}\right] \tag{5a}$$

$$\dot{\varphi}_2 = \frac{1}{C\left(\frac{\Phi_0}{2\pi}\right)^2}\left[\frac{\{a(b_3+b_1)+b_3b_1\}\,q_2 - ab_1q_3 - ab_3q_1}{a(b_1b_2+b_2b_3+b_3b_1)+b_1b_2b_3}\right] \tag{5b}$$

$$\dot{\varphi}_3 = \frac{1}{C\left(\frac{\Phi_0}{2\pi}\right)^2}\left[\frac{\{a(b_1+b_2)+b_1b_2\}\,q_3 - ab_2q_1 - ab_1q_2}{a(b_1b_2+b_2b_3+b_3b_1)+b_1b_2b_3}\right]. \tag{5c}$$

Finally we make one more change of variables in order to make the conjugate variables dimensionless, $q_i = \hbar n_i$, and the Hamiltonian in terms of these variables is:

$$\begin{aligned}
\mathcal{H} &= \frac{1}{2}\vec{q}\cdot\mathbf{M}^{-1}\vec{q} + U(\vec{\varphi}) \\
&= \frac{(2e)^2}{2C}\frac{1}{[a(b_1b_2+b_2b_3+b_3b_1)+b_1b_2b_3]}\times \\
&\left\{(ab_2+ab_3+b_2b_3)n_1^2 + (ab_3+ab_1+b_1b_3)n_2^2 + (ab_1+ab_2+b_2b_1)n_3^2 - 2ab_3n_1n_2 - 2ab_1n_2n_3 - 2ab_2n_1n_3\right\} \\
&- E_J\left[\beta_1\cos(\varphi_1) + \beta_2\cos(\varphi_2) + \beta_3\cos(\varphi_3) + \alpha\cos\left(\varphi_1+\varphi_2+\varphi_3+2\pi\frac{\Phi_{ext}}{\Phi_0}\right)\right].
\end{aligned} \tag{6}$$

2.1.2 Quantum Calculation

So far all the calculations were classical. In order to get the eigenvalues and eigenstates of the quantum problem we need to promote the variables to non-commuting quantum operators $\varphi \to \hat{\varphi}$ and $n \to \hat{n}$. These variables, without hats, will be strictly reserved for numbers and to describe quantum states (when in Dirac bra or ket).
The fact that the variables are conjugates is translated to the relation $\hat{\varphi}_i = -i(\partial/\partial\hat{n}_i)$, and lets us use the charge basis in order to diagonalize the Hamiltonian.
Numeric simulations using this basis are simpler due to the cosine shape of the Josephson energy, since $\cos(\varphi) = (e^{i\varphi} + e^{-i\varphi})/2$ and since $e^{\pm i\hat{\varphi}_i} |n_i\rangle = |n_i \mp 1\rangle$ [16], which makes the Hamiltonian "almost" diagonal, as there are only two types of coupled charge states. The eigenvalue problem is then solved using, e.g., `sparse.linalg.eigs` function, which is included in Python's SciPy package.
The first type of coupled states is two states with a difference of one (charge) in only one of the number variables. This coupling is due to one of the first 3 terms in the Josephson energy, see Eq. 2. The fourth term, however, couples states where there is a charge difference in all three variables simultaneously, and with the same sign, this can be seen by expanding this term,

$$\cos\left(\varphi_1 + \varphi_2 + \varphi_3 + 2\pi\frac{\Phi_{ext}}{\Phi_0}\right) = \frac{1}{2}\left[e^{i\varphi_1}e^{i\varphi_2}e^{i\varphi_3}e^{i2\pi\Phi_{ext}/\Phi_0} + e^{-i\varphi_1}e^{-i\varphi_2}e^{-i\varphi_3}e^{-i2\pi\Phi_{ext}/\Phi_0}\right].$$

The diagonal terms of the Hamiltonian thus correspond to the capacitive energy alone,

$$\langle n_1, n_2, n_3| \mathcal{H} |n_1, n_2, n_3\rangle = \frac{(2e)^2}{2C}\frac{1}{[a(b_1b_2 + b_2b_3 + b_3b_1) + b_1b_2b_3]}\times$$
$$\left\{(ab_2 + ab_3 + b_2b_3)n_1^2 + (ab_3 + ab_1 + b_1b_3)n_2^2 + (ab_1 + ab_2 + b_2b_1)n_3^2 - 2ab_3n_1n_2 - 2ab_1n_2n_3 - 2ab_2n_1n_3\right\}, \tag{7}$$

while the off-diagonal terms correspond to the Josephson energy. The first type of coupled states give

$$\langle n_1, n_2, n_3| \mathcal{H} |n_1 \pm 1, n_2, n_3\rangle = -\frac{\beta_1 E_J}{2} \tag{8a}$$
$$\langle n_1, n_2, n_3| \mathcal{H} |n_1, n_2 \pm 1, n_3\rangle = -\frac{\beta_2 E_J}{2} \tag{8b}$$
$$\langle n_1, n_2, n_3| \mathcal{H} |n_1, n_2, n_3 \pm 1\rangle = -\frac{\beta_3 E_J}{2} \tag{8c}$$

and the second type gives

$$\langle n_1, n_2, n_3| \mathcal{H} |n_1 + 1, n_2 + 1, n_3 + 1\rangle = -\frac{\alpha E_J}{2}e^{i2\pi\Phi_{ext}/\Phi_0} \tag{9a}$$
$$\langle n_1, n_2, n_3| \mathcal{H} |n_1 - 1, n_2 - 1, n_3 - 1\rangle = -\frac{\alpha E_J}{2}e^{-i2\pi\Phi_{ext}/\Phi_0}. \tag{9b}$$

One can easily verify that these components lead indeed to a Hermitian matrix.

We note n_{max} as the maximum state taken into account in the simulation, i.e. $n_i = \{0, \pm1, \pm2, \cdots, \pm n_{max}\}$. In general, the more charge states we use in the numerical diagonalization of the Hamiltonian, the more accurate our eigenstates and eigenvalues will be, but will also make the simulation longer, as the dimension of the Hamiltonian matrix is $(2n_{max} + 1)^3 \times (2n_{max} + 1)^3$.

2.2 Double-Well Energy Landscape

Focusing on the potential energy in Eq. 2 we can look for its stable points in the three-dimensional phase plane. We will only consider the simple case $\beta_1 = \beta_2 = \beta_3 = 1$, and the so-called "sweet spot" where $\Phi_{ext} = \Phi_0/2$ (in which point the qubit is insensitive to flux noise to first order, see below), i.e.

$$-\frac{U}{E_J} = \cos(\varphi_1) + \cos(\varphi_2) + \cos(\varphi_3) + \alpha \cos\left(\varphi_1 + \varphi_2 + \varphi_3 + \pi\right). \tag{10}$$

Looking for extrema, we get upon differentiation the conditions for the phases:

$$\frac{\partial(U/E_J)}{\partial\varphi_1} = \sin(\varphi_1) - \alpha \sin\left(\varphi_1 + \varphi_2 + \varphi_3\right) = 0 \tag{11a}$$

$$\frac{\partial(U/E_J)}{\partial\varphi_2} = \sin(\varphi_2) - \alpha \sin\left(\varphi_1 + \varphi_2 + \varphi_3\right) = 0 \tag{11b}$$

$$\frac{\partial(U/E_J)}{\partial\varphi_3} = \sin(\varphi_3) - \alpha \sin\left(\varphi_1 + \varphi_2 + \varphi_3\right) = 0. \tag{11c}$$

We consider a solution of the form $\varphi_1 \equiv \varphi_2 \equiv \varphi_3 \equiv \varphi^*$, where $\equiv$ stands for equivalence modulo 2π. This solution sets the condition

$$\sin(\varphi^*) - \alpha \sin(3\varphi^*) = 0 \Rightarrow \frac{3\alpha - 1}{4\alpha} = \sin^2(\varphi^*), \tag{12}$$

where we have used the trigonometry identity $\sin(3\theta) = 3\sin(\theta) - 4\sin^3(\theta)$, and excluded the solutions $\sin(\varphi^*) = 0$.
We can see that these solutions for φ^* (four in total) are only valid for $\alpha > 1/3$, in which case the two solutions in the interval $\varphi \in [-\pi, \pi]$ form a double-well potential as the minima of the potential landscape, see Fig 2. In general one seeks to be close to $\alpha = 1/3$ so that the barrier between these wells is not too high.

The application of a magnetic flux that is different from, but close to, $\Phi_0/2$ tilts the previously symmetric double-well potential and favors one of the two states, resulting in the measurement of a net persistent current whose average is different from zero. In Fig 2 we plot this potential for $\Phi_{ext} = 0.5\Phi_0$ and $0.56\Phi_0$. Note that this value is bigger than the usual fluxes used in annealing experiments (see below), but allows us to show a stronger tilt.

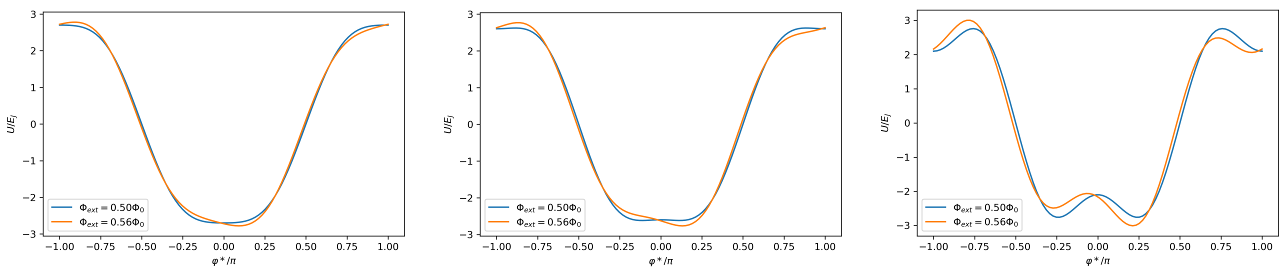

(a) $\alpha = 0.3$ (b) $\alpha = 0.4$ (c) $\alpha = 0.9$

Figure 2: Potential energy as a function of $\varphi*$ for three different α's and under magnetic fluxes $0.5\Phi_0$ (blue line) and $0.56\Phi_0$ (orange line). (a) $\alpha < 1/3$ and so only one minimum exists at $\varphi^* = 0$. (b) $\alpha \gtrsim 1/3$ and so two minima appear close to $\varphi^* = 0$. This is usually the ideal choice for flux qubit. (c) $\alpha \gg 1/3$ and so the two wells are far apart with a high potential barrier between them, located at $\varphi^* = 0$.

2.2.1 Simplified Two-Level Model

Inspired by this double-well landscape, we can build a simplified Hamiltonian that takes into account only two persistent-current states in the vicinity of the flux insensitive point, $\Phi_{ext} = \Phi_0/2$. This Hamiltonian can be written as follows:

$$\mathcal{H} = -\frac{\epsilon}{2}\hat{\sigma}_z - \frac{\Delta}{2}\hat{\sigma}_x. \tag{13}$$

Here, $\hat{\sigma}$ are the sigma Pauli matrices, Δ is the barrier between the wells, i.e. the energy difference at $\Phi_{ext} = \Phi_0/2$, and $\epsilon = 2I_p(\Phi_{\text{ext}} - \Phi_0/2)$, where I_p is the (absolute value of the) persistent-current in the loop, and whose direction determines which well is energetically favored. I_p can be extracted numerically from the slope of the spectrum of the qubit with respect to the magnetic flux.
This Hamiltonian can be diagonalized and give the two eigenenergies with their corresponding (here unnormalized) eigenvectors in the persistent-current basis:

$$E_0 = -\frac{\sqrt{\Delta^2+\epsilon^2}}{2} \qquad |0\rangle = \begin{pmatrix} -\dfrac{\Delta}{\epsilon - \sqrt{\Delta^2+\epsilon^2}} \\ 1 \end{pmatrix} \tag{14a}$$

$$E_1 = \frac{\sqrt{\Delta^2+\epsilon^2}}{2} \qquad |1\rangle = \begin{pmatrix} -\dfrac{\Delta}{\epsilon + \sqrt{\Delta^2+\epsilon^2}} \\ 1 \end{pmatrix}. \tag{14b}$$

Close to the sweet spot ($\epsilon \approx 0$), where the first derivative is zero, the ground and excited energy states are the symmetric and anti-symmetric superpositions of the opposite-signed persistent current states, respectively. For this reason the flux qubit is also sometimes called the *persistent-current qubit* [2, 3].

Full numerical simulation with the values detailed in table 1 leads to the eigenenergies plotted in Fig. 3a. A simplified double-well model's energies, together with the two lowest states of the full simulation is shown in Fig. 3b. We can see that even though the ground state is fairly close to its two-level approximation, the first excited state drifts apart from its approximation. This happens in contrast to the case of the conventional, not capacitively shunted, flux qubit and is due to the strong coupling between this state and the higher energy states, as can be seen in Fig. 3a. In practice, however, the CS4JJ qubit is manipulated very close to the sweet-spot ($\delta\Phi_{ext} < 0.02\Phi_0$), and so the double-well approximation (solid lines in Fig 3b) is justified.

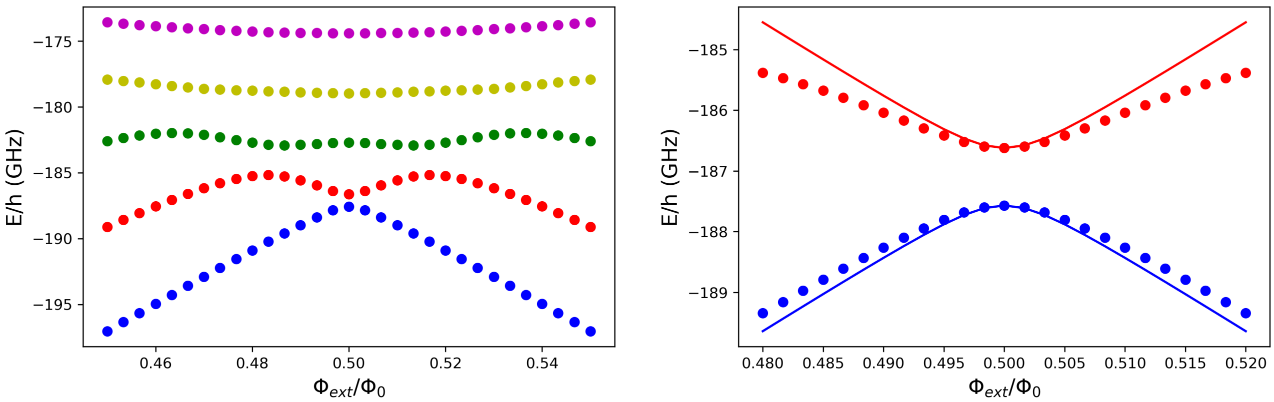

(a) (b)

Figure 3: Simulations of the energy levels of the CS4JJ qubit. (a) First five energy states of the qubit, calculated by full numerical simulation. (b) First two levels in the region $\Phi_{ext} \approx \Phi_0/2$ (circles) and the persistent-current double-well approximation (solid lines). The visible change in the first excited state is due its coupling to higher levels.

Parameter	Symbol	Value [units]
Josephson junction critical current	I_c	0.182 $[\mu A]$
Josephson junction capacitance	C	5.6 $[fF]$
Small Josephson junction area ratio	α	0.4
Big Josephson junctions area ratio	$\beta_1 = \beta_2 = \beta_3$	1
Small Josephson junction capacitance ratio	ζ	≈ 9.1
Big Josephson junctions capacitance ratio	λ	0

Table 1: CS4JJ parameters used in simulations

3 Noise and Decoherence

Mitigating the uncontrolled effect the environment has on the the qubit is a key factor for the progress in quantum information and processing and eventually implementation of quantum algorithms with useful qubits. The time period in which a qubit state holds its expected form is characterized by two rates. T_1 refers to the *relaxation time* of the qubit, i.e. the characteristic time that takes the qubit to decay from its excited state to its ground state. In general, excitation in the opposite direction should be taken into account, but since we work at very low temperatures in which Boltzmann factor is exponentially small ($\sim \exp(-\hbar\omega_q/k_B T)$, where $\hbar\omega_q$ is the energy difference between the states of the qubit and k_B is Boltzmann constant), we neglect it.
Another characteristic time is the *transverse relaxation time*, sometimes referred to simply as the *decoherence time*, and is denoted T_2. It characterizes the period of time in which the phase between the qubit's states is preserved.

In this section we will present the model used by Yan *et al.* in Ref. [17], and use it to simulate the expected T_1 behavior of our qubit.

3.1 Noise Model

Fermi's golden rule quantifies the decay rate from an excited state according to

$$\frac{1}{T_1} = \sum_{\lambda} \frac{1}{\hbar^2} \left| \langle 1| \hat{D}_\lambda |0\rangle \right|^2 S_\lambda(\omega_q). \tag{15}$$

Here, $|0\rangle$ and $|1\rangle$ indicate the ground and excited state of the qubit, respectively, and the sum is over all decay mechanisms taken into account. Here we only discuss flux and charge noise, but decay due to Purcell-enhanced emission to the resonator and quasi-particles tunneling through the Josephson junctions can also be taken into account. Quasi-particles noise mitigation is shortly discussed in Appendix C. $\hat{D}_\lambda$ is the dipole moment related with the specific noise source and $S_\lambda(\omega_q)$ is this noise's (symmetrized) power spectral density at the qubit's frequency. This density can typically be either ohmic, $S_\lambda(\omega) \propto \omega$, or inverse-frequency, $S_\lambda(\omega) \propto 1/\omega^\gamma$. Yan *et al.* investigated 22 C-shunt qubits and built a model that accurately predicted their life-times.

The flux noise relaxation time, T_1^Φ, has the qubit's loop current operator as its dipole operator. We introduce this operator by considering also the self-inductance of the qubit by adding an inductor to the qubit loop. This inductance is much smaller than the qubit's Josephson inductance, and as such was neglected in our previous calculations, but is necessary in order to estimate this dipole operator and evaluate the form

$$\frac{1}{T_1^\Phi} = \frac{1}{\hbar^2} \left| \langle 1| \hat{I}_l |0\rangle \right|^2 S_\Phi(\omega_q), \tag{16}$$

where $\hat{I}_l \equiv (\Phi_0/2\pi)(\hat{\varphi}_L)/L$, φ_L is the phase difference across the loop's inductor and L is the qubit's loop inductance.
In order to numerically evaluate this value we simulate the qubit with one additional phase variable,

the full derivation is given in Appendix A.1. We then use the fact that the phase and charge are conjugate variables, and can thus use the Fourier transform,

$$\langle n|\,\hat{\varphi}\,|n'\rangle = \frac{1}{2\pi}\int_{-\pi}^{\pi}\varphi' e^{-i(n'-n)\varphi'}d\varphi' = \begin{cases} 0 & \text{if } n' = n, \\ i\dfrac{-1^{(n'-n)}}{n'-n} & \text{if } n' \neq n. \end{cases} \tag{17}$$

The charge noise relaxation time, T_1^Q, has the voltage on the superconducting islands as its dipole operator, thus getting the form

$$\frac{1}{T_1^Q} = \frac{1}{\hbar^2}\left|\langle 1|\,\hat{\mathbf{V}}'\,|0\rangle\right|^2 S_Q(\omega_q), \tag{18}$$

where $\hat{\mathbf{V}}' \equiv 2e\hat{n}' \cdot \mathbf{C}^{-1}$, $2e\hat{n}'$ is the charge operator and $\mathbf{C}^{-1}$ is the capacitance matrix of the system in the superconducting islands' charge basis, and both are diagonal in that basis.
We, however, did not use the islands' phase basis in our calculations, instead we have used a change of basis such that our variables were the phase *differences* over the Josephson junctions (and the inductor). This change can be written as $\vec{\varphi} = P\vec{\varphi}'$, or, explicitly

$$\begin{pmatrix} \varphi_1 \\ \varphi_2 \\ \varphi_3 \\ \varphi_L \end{pmatrix} = \begin{pmatrix} 1 & 0 & 0 & 0 \\ -1 & 1 & 0 & 0 \\ 0 & -1 & 1 & 0 \\ 0 & 0 & 0 & -1 \end{pmatrix} \begin{pmatrix} \varphi'_1 \\ \varphi'_2 \\ \varphi'_3 \\ \varphi'_4 \end{pmatrix}, \tag{19}$$

where $\vec{\varphi}'$ is the vector of superconducting wavefunction phases on the superconducting islands (see Fig A.1a).
In our notation the conjugate variables become $\hat{n} = P^{T^{-1}}\hat{n}'$ and the capacitance matrix in our basis becomes the one we have found in Sec 2, $\mathbf{M}^{-1} = P\mathbf{C}^{-1}P^T$. Note that these matrices are thus congruent and hence represent the same quadratic form in their respective bases, i.e. charging energy (cf. Eq. 6).

In Fig. 4a we plot the energies of a qubit with an inductor. These results are with excellent agreement with the results where the self inductance was neglected (up to a constant energy shift, cf. Fig. 3a), and we thus conclude that this approximation is indeed valid. In Fig. 4b the expected relaxation times are plotted as a function of the splitting frequency of the qubit, ω_q. The behavior of the charge noise is not ohmic as expected and was observed by Yan *et al.*, and further investigation (or experimental observations) are needed.

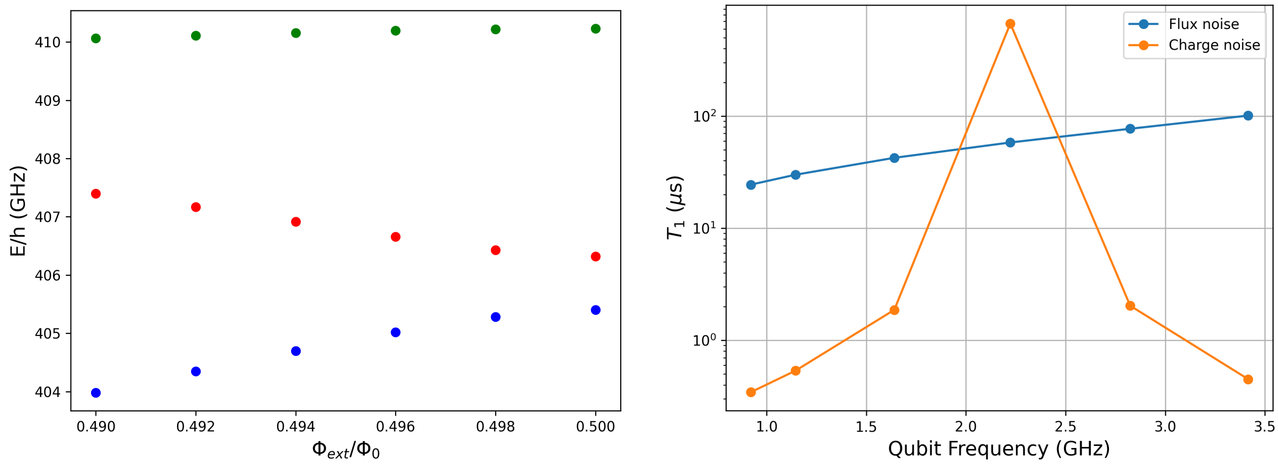

(a) (b)

Figure 4: Simulations of the CS4JJ qubit with its self inductance taken into account. Only limited number of simulation points due to computational demands. (a) First three energy states of the qubit, calculated by full numerical simulation. (b) Relaxation times due to flux and charge noise, as predicted by Eqs. 16 and 18, respectively. The behavior of the charge noise relaxation time is not compatible with previously measured qubits.

4 Control and Readout

In order to control the evolution of the qubit during the run of the algorithm and measure its state at the end of it, superconducting qubits are laid on a chip, comprising different circuitry elements coupled to the qubit and the laboratory equipment. These circuits, which require non-classical quantization and non-linear elements (e.g. Josephson junctions), make the field known as circuit Quantum ElectroDynamics (QED) [18], and is considered to have started with the first experimental observation of strong coupling between a qubit and a resonator [19]. A typical multi-qubits chip usually contains a main feedline, with transmission line resonators coupled to it on one side, and to the qubits on the other side. More control devices can be fabricated as well (e.g. magnetic flux bias lines) and couplers between qubits are necessary if one wants to entangle them or apply multi-qubits quantum gates.

Here we will discuss only the circuit QED elements included in the chip design we were working on and is planned to be fabricated in the near future, once the COVID-19 restrictions are lifted. A schematic circuit diagram of a single (floating) CS4JJ qubit together with its control and readout mechanism is shown in Fig. 5.

The main feedline to which all the qubits' resonators will be coupled is a reflection feedline. That means radio-frequency waves are sent from one end while the other end is shorted to ground. That way the wave is reflected and can be measured on the first end (S11 measurement).
The resonators used in our design are quarter-wavelength transmission line resonators. $\frac{\lambda}{4}$-resonators are shorted to ground on one end and are open on the other end, thus have a (anti-)resonance for frequencies corresponding to four-times their length. These resonances can then be measured by the reflection feedline's response. $\frac{\lambda}{2}$- (or even full-wavelength) resonators are being used in circuit QED as well, but demand more space on the chip. The shorted end in our design is close to the feedline, i.e. zero-potential and inductive coupling between them. The other, open, end of the resonator ends near one of the plates of the qubit's shunt-capacitor, i.e. capacitively coupled to the qubit. A deeper look into the $\frac{\lambda}{4}$-resonators is given in Appendix B.2.

We denote the coupling strength between the qubit and the resonator with g, and their frequency detuning with Δ. The *dispersive regime* is when $|g/\Delta| \ll 1$, where the effective Hamiltonian can be

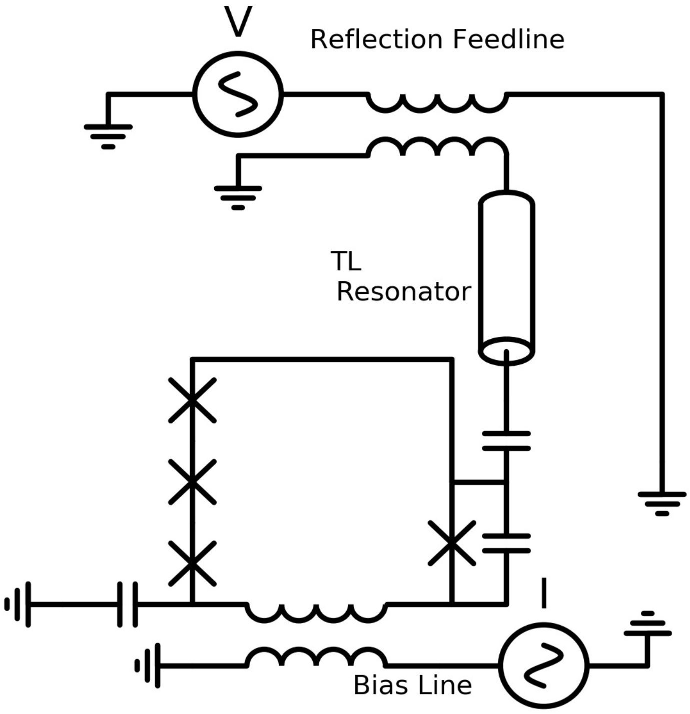

Figure 5: Circuit diagram of the control and readout scheme. A CS4JJ floating qubit is capacitively coupled to a transmission line (TL) resonator, via its shunt-capacitor. The TL resonator is shorted to ground on its other end ($\lambda/4$-resonator) and is inductively coupled to a reflection feedline. Controlling and reading the qubit's state is done by sending RF-waves down that line, and reading the reflection response (S11). The qubits are coupled to resonators with different resonance frequencies for individual state measurements. In addition to a general magnetic flux, applied on the entire chip (not shown), every qubit is coupled to an individual bias line, enabling *in situ* control of the flux threading the specific qubit loop.

written as [19]

$$\mathcal{H} = \hbar \left(\omega_r + \frac{g^2}{\Delta} \hat{\sigma}_z \right) a^\dagger a + \frac{1}{2} \left(\omega_q + \frac{g^2}{\Delta} \right) \hat{\sigma}_z. \tag{20}$$

Here, ω_r is the resonator bare resonance frequency, ω_q is the qubit's frequency, $a^\dagger(a)$ is the resonator's photon creation (annihilation) operator and $\hat{\sigma}_z$ is the Pauli matrix acts on the qubit's truncated two-level approximation, in its energy basis.
The resonance frequency of the resonator therefore depends on the qubit's energy state. This change can be seen in the measurements of the reflection line response. We can also see that the qubit's energy separation changes due to its coupling to the resonator, and thus the signal needed to excite the qubit is different too, although still sufficiently detuned from the resonator resonance frequency.
Measurements in the persistent-current direction basis (usually using a SQUID magnetometer, see Ref [4]) are also possible, and even necessary in the case of quantum-annealing experiments, but are outside the scope of this report.

Lastly, every qubit was coupled to a bias line, allowing an individual control of the magnetic flux threading it. Note that in the case of the grounded CS4JJ qubits this coupling is galvanic. Controlling this flux allows *in situ* control of the qubit's frequency and thus control over the phase acquired. This can be thought of as a $\hat{\sigma}_z$ gate (whereas qubit excitation by using the resonator is a $\hat{\sigma}_x$ gate).

5 Coupling

A single qubit is not very useful for quantum computing tasks. In order to achieve some kind of quantum computational advantage, many qubits need to be entangled [20]. This entanglement implies that they must be coupled among themselves in a controlled manner. Even though a direct coupling between two flux qubits is possible and useful for gate-based quantum computing [21], in the case of quantum annealing we wish to implement problems in Ising-like adiabatically time-dependent Hamiltonians and therefore need a *tunable* coupler.
Many superconducting elements and coupling techniques have been proposed and implemented in recent years, including the dc-SQUID [22], galvanic coupling to an rf-SQUID [23, 24], or inductive coupling to a compound Josephson junction rf-SQUID [25], and also galvanic coupling to a third flux qubit [26, 27].

In this section, we will look into the semi-classical mathematical description of two coupled qubits (which can be easily generalized to an arbitrary number of qubits) and then discuss in details the rf-SQUID coupler, which is a promising candidate for tunable coupling.

5.1 Mathematical Description

We begin by considering a simpler system of two loops, denoted A and B, that are directly (without a coupler) coupled with a mutual inductance M, as shown in Fig. 6a. Their interaction term is thus

$$\mathcal{H}_{int} = MI^A I^B, \tag{21}$$

where $I^{A(B)}$ is the current circulating in loop $A(B)$.
Note that this term is true for non-galvanic coupling between the loops, i.e. no shared current wire. A generalization for the case of galvanic coupling can be made [23] by substituting $M \to \tilde{M}(M, L_A, L_B)$, where $L_{A(B)}$ is the inductance of loop $A(B)$.

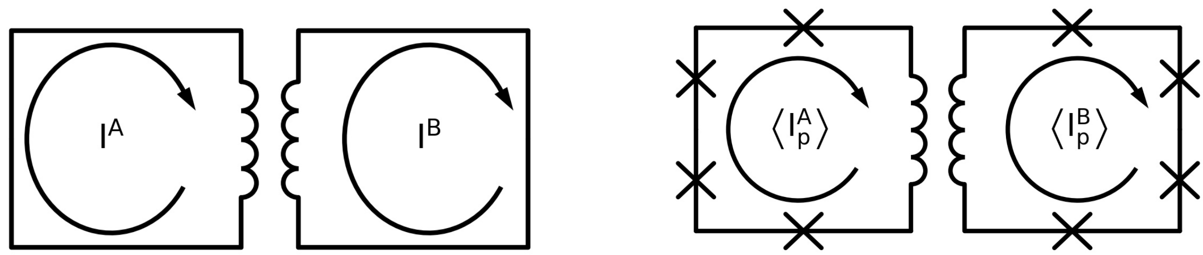

(a) Current loops (b) Flux qubits

Figure 6: Inductively coupled (a) current loops and (b) flux qubits. In both cases the coupling is direct and does not include a mediator. The coupling terms are therefore similar except for the identification of the currents circulating in the flux qubits as persistent currents.

In the case of flux qubits and within the vicinity of the flux-insensitive point, where the double-well approximation is valid (see Sec. 2.2), this circulating current is the average persistent current which takes the form $\hat{I} = I_p \hat{\sigma}_z$, where $\hat{\sigma}_z = \pm 1$ according to the persistent current's direction, see Fig. 6b. The full Hamiltonian for two directly-inductively-coupled qubits is then

$$\mathcal{H} = -\sum_{i=A,B} \left(\frac{\epsilon^{(i)}}{2} \hat{\sigma}_z^{(i)} + \frac{\Delta^{(i)}}{2} \hat{\sigma}_x^{(i)} \right) + MI_p^A I_p^B \hat{\sigma}_z^A \hat{\sigma}_z^B. \tag{22}$$

The next step we make is to add a simple mediator between the qubits in the form of a current loop, see Fig. 7a. This mediator shares a mutual inductance M with each qubit. Change in the

persistent current in qubit $A(B)$ will therefore change the magnetic flux threading the loop according to $\delta\Phi_C = MI_p^{A(B)}$. This change will affect the current circulating in the loop, such that $\delta I^C = \delta\Phi_C/L = (M/L)\delta I^{A(B)}$, where L is the self inductance of the current loop. Finally, this will affect the flux threading qubit $B(A)$ and we arrive at an effective mutual inductance between the qubits $M_{\text{eff}} = M^2/L$.
Note that since L is positive by definition, the interaction term can cause only anti-ferromagnetic behavior. It is therefore needed to add a tunable mediator, capable of controlling the interaction term, turn it on and off and switch it from positive (anti-ferromagnetic behavior) to negative (ferromagnetic behavior).

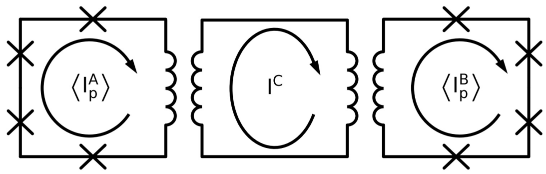

(a) Current loop coupler

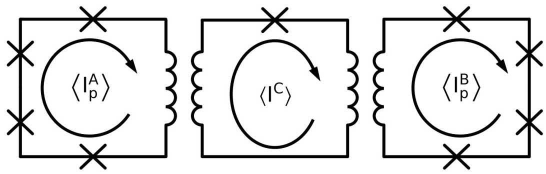

(b) rf-SQUID coupler

Figure 7: Inductively coupled flux qubits via (a) a simple current loop and (b) an rf-SQUID coupler. This mediated coupling allows controlling of the effective mutual inductance and in particular makes it tunable and therefore useful for quantum annealing purposes.

5.2 rf-SQUID Coupler

An rf-SQUID is basically a superconducting current loop with a single Josephson junction (see Fig. 7b). Here we will derive its effective self inductance and show that it can be controlled by changing the magnetic flux threading it, giving the final coupling term

$$J = I_p^2 M^2 \frac{1}{L_{\text{eff}}}, \tag{23}$$

where we have compared the qubit-rf-SQUID-qubit Hamiltonian to that of the Ising model,

$$\mathcal{H} = -\sum_{i=A,B} \left(\frac{\epsilon^{(i)}}{2} \hat{\sigma}_z^{(i)} + \frac{\Delta^{(i)}}{2} \hat{\sigma}_x^{(i)} \right) + J \hat{\sigma}_z^A \hat{\sigma}_z^B. \tag{24}$$

Note that we assumed $I_p^A = I_p^B = I_p$ for simplicity.

The rf-SQUID's circuit is simpler than that of the CS4JJ qubit and we model it as a Josephson junction and an inductor connected in series, see Fig A.1b. The phase quantization and the phase-to-current Josephson relation give the following set of equations:

$$\varphi_L + \varphi_J = 2\pi \frac{\Phi_{\text{ext}}}{\Phi_0} \tag{25a}$$

$$\varphi_L = \frac{2\pi}{\Phi_0} IL \tag{25b}$$

$$I = I_c \sin(\varphi_J), \tag{25c}$$

where L is the rf-SQUID's self-inductance, φ_L is the phase difference caused by it, I_c is the Josephson junction's critical current and φ_J is the phase difference caused by it.
All together this leads us to the current circulating in the rf-SQUID, i.e. the solution to the equation

$$I^* = I_c \sin\left(2\pi \frac{\Phi_{\text{ext}} - I^* L}{\Phi_0} \right). \tag{26}$$

This result is to be compared to another familiar way to calculate the current, $\langle \hat{I} \rangle = \partial \langle \hat{E} \rangle / \partial \Phi_{\text{ext}}$, where $\hat{E}$ is the energy operator. In fact, they are equal when we disregard the capacitive energy of the Hamiltonian, which in the case of its ground state is reasonable approximation.
In order to find this value we start by finding the Hamiltonian of the system in a similar manner to the calculations done in Sec. 2.1. It is found to be

$$\mathcal{H} = \left(\frac{\Phi_0}{2\pi}\right)^2 \frac{C}{2}\dot{\varphi}_L^2 + \left(\frac{\Phi_0}{2\pi}\right)^2 \frac{1}{2L}\varphi_L^2 - E_J \cos\left(\varphi_L - 2\pi\frac{\Phi_{\text{ext}}}{\Phi_0}\right). \tag{27}$$

This Hamiltonian is then diagonalized (see Appendix A.2 for detailed derivations and simulation parameters) in order to find its eigenstates. The two lowest are shown in Fig. 8a. Notice the big gap between them ($> 70\ GHz \gg \omega_q$, the frequency gap of the qubit). This gap allows us to consider the ground state of the rf-SQUID as the only pertinent one. We then differentiate this ground energy with respect to the applied flux, twice.
The first derivative is the current, giving practically same results as the one solving Eq. 26 (comparison is made in Fig. 8b). Differentiating this current one more time gives the susceptibility of the rf-SQUID to magnetic field,

$$\frac{\partial \langle \hat{E}_0 \rangle}{\partial \Phi_{\text{ext}}} = \langle \hat{I} \rangle \qquad\qquad \frac{\partial^2 \langle \hat{E}_0 \rangle}{\partial \Phi_{\text{ext}}^2} = \chi \equiv \frac{1}{L_{\text{eff}}}, \tag{28}$$

where L_{eff} is named the effective inductance of the rf-SQUID and is the tunable part of the coupling energy. This term can be either positive or negative in a broad region of magnitudes (see Fig. 8b), and can thus help us execute annealing algorithms.

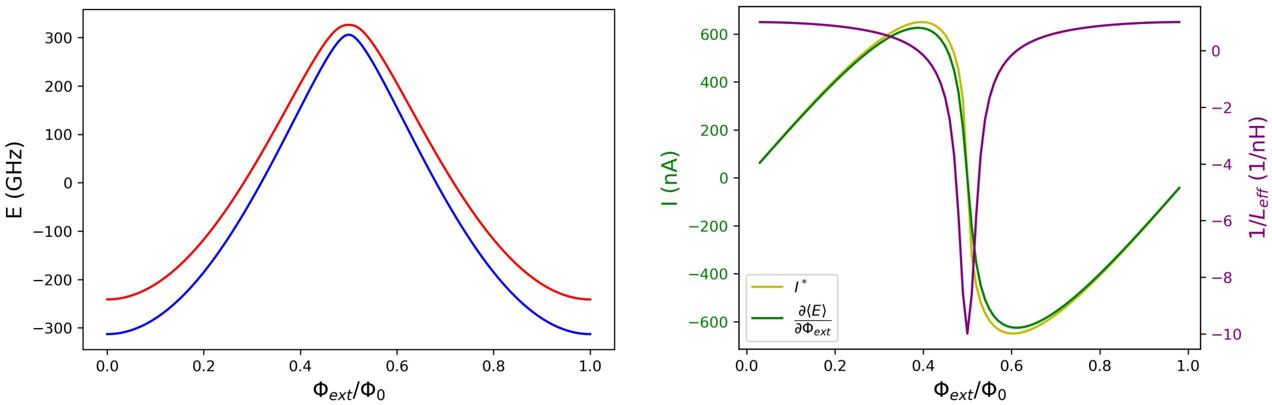

(a) (b)

Figure 8: Simulations of rf-SQUID. (a) Two lowest-energy levels of the rf-SQUID as a function of the magnetic flux threading it. As a coupler it is important to keep it in the ground state, which is achieved by designing it with a big energy gap (compared to the qubits' gap) between the states. (b) The current flowing in the rf-SQUID, calculated using the energy derivative (green) and the equation solver technique (yellow) for comparison. The inverse effective inductance (purple) is shown too, calculated by the second energy derivative with respect to the flux. Notice the change in its value, especially between positive and negative values. See Appendix A.2 for simulation parameters.

It is interesting to note that even without solving the Hamiltonian, an analytic expression can also be given. Using Eqs. 25 and 26 we get:

$$\frac{1}{L_{\text{eff}}} \equiv \frac{\partial I^*}{\partial \Phi_{\text{ext}}} = \frac{1}{L}\frac{\beta\cos(\varphi_J)}{1 + \beta\cos(\varphi_J)}, \tag{29}$$

where $\beta = L/L_J = (2\pi/\Phi_0)LI_c$, since $L_J = \Phi_0/2\pi I_c$ is the Josephson inductance.

6 Sample Design and Simulation

In this section we will discuss the design and simulations of non-coupled multi-qubit sample planned to be fabricated in the university of Glasgow once the COVID-19 restrictions are lifted. This collaboration is part of the AVaQus project, towards a European coherent quantum annealer.
The sample includes eight CS4JJ qubits, together with individual flux bias-lines and $\frac{\lambda}{4}$-resonators with different resonance frequencies, to allow individual state readout. The resonators are inductively coupled to a main reflection feedline. Four qubits have floating CS4JJ design and four are have grounded CS4JJ design). The layout of the full chip is shown in Fig 9, together with magnifications of the designs of both qubits and their coupling to a resonator.

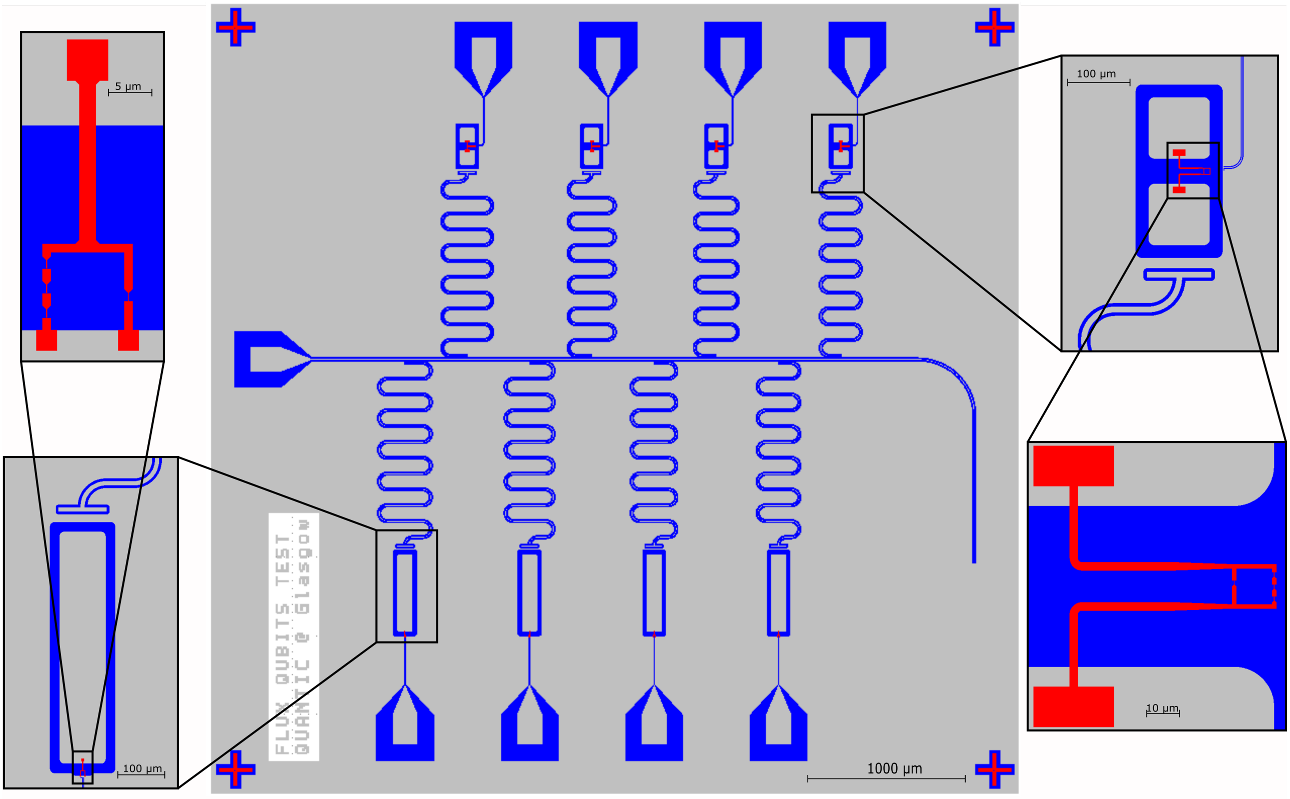

Figure 9: Full chip. The ground plane and all the metallic circuit QED elements are illustrated in grey, in contrast with the exposed substrate, in blue. On the left (right) there are zoom-in figures of a grounded (floating) qubit loop, its capacitor plate(s) and its coupling to the resonator. Qubit loops and its wire connections to other elements are shown in red.

6.1 Design Parameters

The metal chosen for the circuit QED elements and the qubit loops is aluminum, known as "the silicon of superconductivity"[28]. Aluminum becomes a superconductor under $T_c \approx 1.2\ K$ and was shown to display high quality factor resonators [29], thus promising high coherence time and efficient control and readout for the qubit.
The substrate on which the aluminum will be deposited is 500 μm-height silicon. This material has a relatively high dielectric constant ($\epsilon_r \approx 11.9$) and low loss-tangent (≈ 0.004), thus enabling the fabrication of more compact capacitors and resonators, and with high internal quality factor Q_i (see Appendix B.2).

The coplanar waveguide (CPW) geometry is widely used in circuit QED, as it allows strong coupling between qubits and resonators and provides a clean environment to the qubits. More specifically,

ground planes screen electrical fields between elements that are not close to each other, and have proven to be a mitigating method against flux noise [30]. Further discussion of the CPW properties is given in Appendix B.
The circuit QED elements (with the exclusion of the qubit loops) are therefore metallized with a gap between them and a ground plane which covers almost the entire chip. The ratio between the linewidth and and this gap should stay constant in order to maintain constant characteristic impedance (see Appendix B). Since we aim for impedance matching $Z_0 \sim 50\ \Omega$ [31], and considering the substrate's height and its relative permittivity, a ratio of $W = 2S$ was chosen, where W is the linewidth and S is the exposed spacing between the line and the ground plane.
Feedline and resonators width was chosen so it could accommodate a high enough RF-current while staying compact, but the bias-lines can be narrower. Widths $W = 10\ \mu m$ and $2\ \mu m$, corresponding to $S = 5\ \mu m$ and $1\ \mu m$ were therefore chosen for the design.

Qubit wire width and loop parameters were chosen according to the same guidelines, while taking into account that smaller perimeter and wider wires were shown to improve the qubit's coherence time [32]. The qubit loop is therefore squared with wire width equal to $1\ \mu m$ and the distance from the center of one wire to the center of the opposite loop wire is $10\ \mu m$.

6.2 Simulations

Numerical simulations of the qubit's energy levels, persistent-currents and noise decoherence using Hamiltonian diagonalization in Python were already discussed in sections 2 and 3. These simulations allow us to predict the properties of the qubit and change its parameters accordingly. Here we discuss the simulations done prior to the actual fabrication in order to predict the general behavior of the sample. These simulations are critical in order to avoid an exhausting trial-and-error process and save resources.

The magnetic inductance of the wires was estimated using the program FastHenry. FastHenry takes into accound both geometrical and kinetic inductance and calculates the impedance of the wires by numerically solving the Maxwell-London equations for a given penetration depth [33].
Capacitance matrices were found using several programs, FasterCap, COMSOL and Sonnet. All of these programs are capable of numerically finding these matrices for coplanar elements, using different methods. Their results are then compared for verification.

Finally, Sonnet is able to predict resonances in the chip, and allows us to know if they are indeed spaced enough to allow individual qubit measurements. It also allows us to quantify the coupling strength between the feedline and resonator is such that this readout is fast enough while conserving a small dissipation rate (due to the loaded quality factor, see Appendix B.3).

References

[1] Richard P Feynman. Simulating physics with computers. *International Journal of Theoretical Physics*, 21(6/7), 1982.

[2] JE Mooij, TP Orlando, Lin Tian, Caspar H van der Wal, LS Levitov, Seth Lloyd, and JJ Mazo. A superconducting persistent current qubit. *Science*, 285:1036, 1999.

[3] T. Orlando, J. Mooij, Lin Tian, Caspar van der Wal, L. Levitov, Seth Lloyd, and Juan Mazo. Superconducting persistent-current qubit. *Physical Review B*, 60:15398, 08 1999. doi: 10.1103/PhysRevB.60.15398.

[4] Sergey Novikov, Robert Hinkey, Steven Disseler, James I Basham, Tameem Albash, Andrew Risinger, David Ferguson, Daniel A Lidar, and Kenneth M Zick. Exploring more-coherent quantum annealing. In *2018 IEEE International Conference on Rebooting Computing (ICRC)*, pages 1–7. IEEE, 2018.

[5] Tadashi Kadowaki and Hidetoshi Nishimori. Quantum annealing in the transverse ising model. *Physical Review E*, 58(5):5355, 1998.

[6] Edward Farhi, Jeffrey Goldstone, Sam Gutmann, and Michael Sipser. Quantum computation by adiabatic evolution. *arXiv preprint quant-ph/0001106*, 2000.

[7] Giuseppe E Santoro, Roman Martoňák, Erio Tosatti, and Roberto Car. Theory of quantum annealing of an ising spin glass. *Science*, 295(5564):2427–2430, 2002.

[8] Roman Martoňák, Giuseppe E Santoro, and Erio Tosatti. Quantum annealing of the traveling-salesman problem. *Physical Review E*, 70(5):057701, 2004.

[9] John Preskill. Quantum computing in the nisq era and beyond. *Quantum*, 2:79, 2018.

[10] Jerry Robinson-George Roussos Ira Schnapp Jack Schiff, Bob Kane and Whitney Ellsworth. Batman: "case of the costume-clad killers". *Detective Comics*, 1(60), 1942.

[11] J. Q. You, Xuedong Hu, S. Ashhab, and Franco Nori. Low-decoherence flux qubit. *Phys. Rev. B*, 75:140515, Apr 2007. doi: 10.1103/PhysRevB.75.140515. URL https://link.aps.org/doi/10.1103/PhysRevB.75.140515.

[12] GJ Dolan. Offset masks for lift-off photoprocessing. *Applied Physics Letters*, 31(5):337–339, 1977.

[13] David P DiVincenzo, Patrice Bertet, Irinel Chiorescu, JE Mooij, and Guido Burkard. Asymmetry and decoherence in a double-layer persistent-current qubit. *Physical Review/B*, 71, 2005.

[14] Brian Josephson. Possible new effect in superconducting tunneling. *Phys. Lett.*, 1:251–253, 1962.

[15] Steven M Girvin. Circuit qed: superconducting qubits coupled to microwave photons. *Quantum Machines: Measurement and Control of Engineered Quantum Systems*, 113:2, 2011.

[16] Francesco Tafuri. *Fundamentals and Frontiers of the Josephson Effect*, volume 286. Springer Nature, 2019.

[17] Fei Yan, Simon Gustavsson, Archana Kamal, Jeffrey Birenbaum, Adam P Sears, David Hover, Ted J Gudmundsen, Danna Rosenberg, Gabriel Samach, Steven Weber, et al. The flux qubit revisited to enhance coherence and reproducibility. *Nature communications*, 7(1):1–9, 2016.

[18] Alexandre Blais, Arne L Grimsmo, SM Girvin, and Andreas Wallraff. Circuit quantum electrodynamics. *arXiv preprint arXiv:2005.12667*, 2020.

[19] Andreas Wallraff, David I Schuster, Alexandre Blais, Luigi Frunzio, R-S Huang, Johannes Majer, Sameer Kumar, Steven M Girvin, and Robert J Schoelkopf. Strong coupling of a single photon to a superconducting qubit using circuit quantum electrodynamics. *Nature*, 431(7005):162–167, 2004.

[20] Michael A Nielsen and Isaac L Chuang. *Quantum Computation and Quantum Information*. Cambridge University Press, 2010.

[21] Pieter Cristiaan De Groot. *Coupled flux qubits and double bifurcation readout*. PhD thesis, TU Delft, 2010.

[22] Travis Hime, PA Reichardt, BLT Plourde, TL Robertson, C-E Wu, AV Ustinov, and John Clarke. Solid-state qubits with current-controlled coupling. *science*, 314(5804):1427–1429, 2006.

[23] Steven J. Weber, Gabriel O. Samach, David Hover, Simon Gustavsson, David K. Kim, Alexander Melville, Danna Rosenberg, Adam P. Sears, Fei Yan, Jonilyn L. Yoder, William D. Oliver, and Andrew J. Kerman. Coherent coupled qubits for quantum annealing. *Phys. Rev. Applied*, 8: 014004, Jul 2017. doi: 10.1103/PhysRevApplied.8.014004. URL https://link.aps.org/doi/10.1103/PhysRevApplied.8.014004.

[24] Alec Maassen van den Brink, AJ Berkley, and M Yalowsky. Mediated tunable coupling of flux qubits. *New Journal of Physics*, 7(1):230, 2005.

[25] R Harris, T Lanting, AJ Berkley, J Johansson, MW Johnson, P Bunyk, E Ladizinsky, N Ladizinsky, T Oh, and Siyuan Han. Compound josephson-junction coupler for flux qubits with minimal crosstalk. *Physical Review B*, 80(5):052506, 2009.

[26] M. Grajcar, Yu-xi Liu, Franco Nori, and Alexandre Zagoskin. Switchable resonant coupling of flux qubits. *Physical Review B*, 74, 05 2006. doi: 10.1103/PhysRevB.74.172505.

[27] SHW Van der Ploeg, A Izmalkov, Alec Maassen van den Brink, U Hübner, M Grajcar, E Il'Ichev, H-G Meyer, and AM Zagoskin. Controllable coupling of superconducting flux qubits. *Physical review letters*, 98(5):057004, 2007.

[28] John M Martinis, Michel H Devoret, and John Clarke. Quantum josephson junction circuits and the dawn of artificial atoms. *Nature Physics*, 16(3):234–237, 2020.

[29] William D Oliver and Paul B Welander. Materials in superconducting quantum bits. *MRS bulletin*, 38(10):816–825, 2013.

[30] T Lanting, AJ Berkley, B Bumble, P Bunyk, A Fung, J Johansson, A Kaul, A Kleinsasser, E Ladizinsky, F Maibaum, et al. Geometrical dependence of the low-frequency noise in superconducting flux qubits. *Physical Review B*, 79(6):060509, 2009.

[31] David M Pozar. *Microwave engineering*. John Wiley & Sons, 2009.

[32] Jochen Braumüller, Leon Ding, Antti Vepsäläinen, Youngkyu Sung, Morten Kjaergaard, Tim Menke, Roni Winik, David Kim, Bethany M Niedzielski, Alexander Melville, et al. Characterizing and optimizing qubit coherence based on squid geometry. *arXiv preprint arXiv:2002.09372*, 2020.

[33] Michael Tinkham. *Introduction to superconductivity*. Courier Corporation, 2004.

[34] Ramamurti Shankar. *Principles of quantum mechanics*. Springer Science & Business Media, 2012.

[35] W Witschel. Harmonic oscillator integrals by operator methods, a simple unified approach. *European Journal of Physics*, 17(6):357, 1996.

[36] Rainee N Simons. *Coplanar waveguide circuits, components, and systems*, volume 165. John Wiley & Sons, 2004.

[37] Spartak Gevorgian, LJ Peter Linner, and Erik L Kollberg. Cad models for shielded multilayered cpw. *IEEE transactions on microwave theory and techniques*, 43(4):772–779, 1995.

[38] Antti Vepsäläinen, Amir H Karamlou, John L Orrell, Akshunna S Dogra, Ben Loer, Francisca Vasconcelos, David K Kim, Alexander J Melville, Bethany M Niedzielski, Jonilyn L Yoder, et al. Impact of ionizing radiation on superconducting qubit coherence. *arXiv preprint arXiv:2001.09190*, 2020.

[39] Laura Cardani, Francesco Valenti, Nicola Casali, Gianluigi Catelani, Thibault Charpentier, Massimiliano Clemenza, Ivan Colantoni, Angelo Cruciani, Luca Gironi, Lukas Grünhaupt, Daria Gusenkova, Fabio Henriques, Marc Lagoin, Maria Martinez, Giorgio Pettinari, Claudia Rusconi, Oliver Sander, Alexey V. Ustinov, Marc Weber, Wolfgang Wernsdorfer, Marco Vignati, Stefano Pirro, and Ioan M. Pop. Reducing the impact of radioactivity on quantum circuits in a deep-underground facility. *arXiv preprint arXiv:2005.02286*, 2020.

Appendices

A Additional Hamiltonians

A.1 C-shunt Flux Qubit with Self Inductance

In order to model the flux noise impact on the qubit we have to consider its magnetic inductance (see 3, previously neglected because it is several orders of magnitude smaller than the Josephson inductance of the qubit, $L_J \sim (\Phi_0/2\pi)/I_c$, and does not affect the qubit's spectrum. This inductance is modeled as an inductor connected in series with the Josephson junctions.
We follow the steps taken in the flux qubit without inductance (see main text, Sec. 2.1), and get the (slightly different) capacitive energy,

$$T(\vec{\varphi}) = \frac{C}{2}\left(\frac{\Phi_0}{2\pi}\right)^2 \left[\dot{\varphi}_1^2 + \dot{\varphi}_2^2 + \dot{\varphi}_3^2 + a\left(\dot{\varphi}_1 + \dot{\varphi}_2 + \dot{\varphi}_3 + \dot{\varphi}_L\right)^2\right]. \tag{A.1}$$

Here, some parameters are omitted (cf Eq. 1) according to $a = \alpha + \zeta$, $\lambda = 0$, $\beta_i = 1\ \forall i$, and a new variable related to the phase difference across the inductor, φ_L, is introduced. We also used the quantization condition, $\sum_i \varphi_i + 2\pi(\Phi_{ext}/\Phi_0) = 2\pi n,\ n \in \mathbb{N}$. The model circuit is shown in Fig. A.1a. By dropping the constants we get the total potential energy, comprising Josephson energy and inductance energy,

$$U(\vec{\varphi}) = -E_J\left[\cos(\varphi_1) + \cos(\varphi_2) + \cos(\varphi_3) + \alpha\cos\left(\varphi_1 + \varphi_2 + \varphi_3 + \varphi_L + 2\pi\frac{\Phi_{ext}}{\Phi_0}\right)\right] + \left(\frac{\Phi_0}{2\pi}\right)^2 \frac{\varphi_L^2}{2L}. \tag{A.2}$$

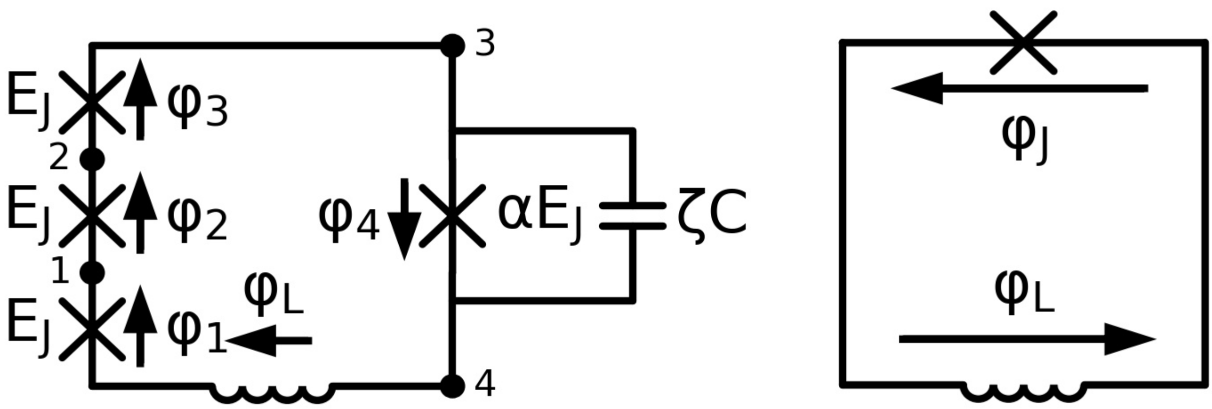

(a) (b)

Figure A.1: Circuit diagrams of (a) capacitively-shunted four Josephson junctions flux qubit, where the inductance is taken into account and (b) rf-SQUID. Small arrows indicate the phase-differences over circuit elements (Josephson junctions and inductors) and their sign convention, used as the variables for the circuits' quantization. Dots indicate superconducting islands (see main text).

The conjugate variables of the Lagrangian $\mathcal{L} = T\left(\dot{\vec{\varphi}}\right) - U(\vec{\varphi})$ are

$$\begin{pmatrix} q_1 \\ q_2 \\ q_3 \\ q_L \end{pmatrix} = \begin{pmatrix} \frac{\partial \mathcal{L}}{\partial \dot{\varphi}_1} \\ \frac{\partial \mathcal{L}}{\partial \dot{\varphi}_2} \\ \frac{\partial \mathcal{L}}{\partial \dot{\varphi}_3} \\ \frac{\partial \mathcal{L}}{\partial \dot{\varphi}_L} \end{pmatrix} = C\left(\frac{\Phi_0}{2\pi}\right)^2 \begin{pmatrix} 1+a & a & a & a \\ a & 1+a & a & a \\ a & a & 1+a & a \\ a & a & a & a \end{pmatrix} \begin{pmatrix} \dot{\varphi}_1 \\ \dot{\varphi}_2 \\ \dot{\varphi}_3 \\ \dot{\varphi}_L \end{pmatrix} = \mathbf{M} \begin{pmatrix} \dot{\varphi}_1 \\ \dot{\varphi}_2 \\ \dot{\varphi}_3 \\ \dot{\varphi}_L \end{pmatrix}. \tag{A.3}$$

Finally we make one more change to make the conjugate variables dimensionless according to $q_i = \hbar n_i$ and the Hamiltonian in terms of these variables is:

$$\begin{aligned} \mathcal{H} &= \frac{1}{2}\vec{q} \cdot \mathbf{M}^{-1}\vec{q} + U(\vec{\varphi}) \\ &= \frac{(2e)^2}{2C}\left[n_1^2 + n_2^2 + n_3^2 - 2n_1 n_L - 2n_2 n_L - 2n_3 n_L + \frac{3a+1}{a} n_L^2\right] \\ &- E_J\left[\cos(\varphi_1) + \cos(\varphi_2) + \cos(\varphi_3) + \alpha\cos\left(\varphi_1 + \varphi_2 + \varphi_3 + \varphi_L + 2\pi\frac{\Phi_{ext}}{\Phi_0}\right)\right] + \left(\frac{\Phi_0}{2\pi}\right)^2 \frac{\varphi_L^2}{2L}. \end{aligned} \tag{A.4}$$

Note that in the limit $\varphi_L, \dot{\varphi}_L \to 0$ we indeed get the familiar result for the flux qubit with zero inductance (Eq. 6).

The capacitive energy of the Hamiltonian thus correspond to diagonal terms,

$$\langle n_1, n_2, n_3, n_L| \mathcal{H} |n_1, n_2, n_3, n_L\rangle = \frac{(2e)^2}{2C}\left[n_1^2 + n_2^2 + n_3^2 - 2n_1 n_L - 2n_2 n_L - 2n_3 n_L + \frac{3a+1}{a} n_L^2\right], \tag{A.5}$$

while the off-diagonal terms correspond to the Josephson and inductance energies. The first type of coupled states give

$$\langle n_1, n_2, n_3, n_L| \mathcal{H} |n_1 \pm 1, n_2, n_3, n_L\rangle = -\frac{E_J}{2} \tag{A.6a}$$

$$\langle n_1, n_2, n_3, n_L| \mathcal{H} |n_1, n_2 \pm 1, n_3, n_L\rangle = -\frac{E_J}{2} \tag{A.6b}$$

$$\langle n_1, n_2, n_3, n_L| \mathcal{H} |n_1, n_2, n_3 \pm 1, n_L\rangle = -\frac{E_J}{2} \tag{A.6c}$$

and the second type gives

$$\langle n_1, n_2, n_3, n_L| \mathcal{H} |n_1 + 1, n_2 + 1, n_3 + 1, n_L + 1\rangle = -\frac{\alpha E_J}{2} e^{+i2\pi\Phi_{ext}/\Phi_0} \tag{A.7a}$$

$$\langle n_1, n_2, n_3, n_L| \mathcal{H} |n_1 - 1, n_2 - 1, n_3 - 1, n_L - 1\rangle = -\frac{\alpha E_J}{2} e^{-i2\pi\Phi_{ext}/\Phi_0}. \tag{A.7b}$$

The third and last type is related to the inductance term, and is a bit more delicate to deal with. In order to calculate the matrix element $\langle n_L| \hat{\varphi}_L^2 |n_L'\rangle$ we use the fact that these are conjugate variables and thus are the Fourier transform of each other, giving

$$\langle n| \hat{\varphi}^2 |n'\rangle = \frac{1}{2\pi}\int_{-\pi}^{\pi} \varphi'^2 e^{-i(n'-n)\varphi'} d\varphi' = \begin{cases} \dfrac{\pi^2}{3} & \text{if } n' = n, \\ 2\dfrac{-1^{|n'-n|}}{|n'-n|^2} & \text{if } n' \neq n. \end{cases} \tag{A.8}$$

Note the finite limits of the integral, taken since n is still taken to be discrete, and hence φ is compact (periodic). This approximation is valid if the wavefunction goes to zero near the first Brillouin zone boundaries [15]. In our case the characteristic inductance energy is two orders of magnitude larger than the Josephson energy (and three orders of magnitude larger than the capacitive energy) and so this approximation holds.

We can thus express this type of matrix elements:

$$\langle n_1, n_2, n_3, n_L | \mathcal{H} | n_1, n_2, n_3, n_L \rangle = \frac{\pi^2}{6L}\left(\frac{\Phi_0}{2\pi}\right)^2 \tag{A.9a}$$

$$\langle n_1, n_2, n_3, n_L | \mathcal{H} | n_1, n_2, n_3, n'_L \rangle = \frac{1}{L}\left(\frac{\Phi_0}{2\pi}\right)^2 \frac{-1^{|n'_L - n_L|}}{|n'_L - n_L|^2}, \tag{A.9b}$$

where the diagonal term is *added* to the previous one (Eq. A.5), and the second one only holds for the non-diagonal terms. In practice only some of the non-diagonal terms are kept in the numerical simulations in order to keep the matrix sparse. A convergence test was made in order to determine this limit.
One can easily verify that these components lead indeed to a Hermitian matrix.

A.2 rf-SQUID

[1] rf-SQUID is a promising candidate for the tunable coupling of two flux-qubits, see Sec. 5.2. From its circuit, shown in Fig. A.1b, we arrive directly at the Hamiltonian,

$$\mathcal{H} = \left(\frac{\Phi_0}{2\pi}\right)^2 \frac{C}{2}\dot{\varphi}_L^2 + \left(\frac{\Phi_0}{2\pi}\right)^2 \frac{1}{2L}\varphi_L^2 - E_J \cos\left(\varphi_L - 2\pi\frac{\Phi_{\text{ext}}}{\Phi_0}\right). \tag{A.10}$$

Looking only at the first two terms, one can recognize the Hamiltonian of a harmonic oscillator and thus write this Hamiltonian as

$$\mathcal{H} = \frac{p^2}{2m} + \frac{1}{2}m\omega^2\varphi_L^2 - E_J \cos\left(\varphi_L - 2\pi\frac{\Phi_{\text{ext}}}{\Phi_0}\right) \tag{A.11}$$

$$p = \frac{\partial \mathcal{L}}{\partial \dot{\varphi}} = \left(\frac{\Phi_0}{2\pi}\right)^2 C\dot{\varphi}, \tag{A.12}$$

where we made the following change of variables:

$$E_C \equiv \frac{e^2}{2C} \tag{A.13a}$$

$$\beta_L \equiv \frac{L}{L_J} = \frac{2\pi L}{\Phi_0} I_c \tag{A.13b}$$

$$m = \frac{\hbar}{8E_C} \tag{A.13c}$$

$$\omega = \frac{2E_C}{\hbar}\sqrt{\frac{2E_J}{\beta_L E_C}}. \tag{A.13d}$$

The eigenstates for the harmonic Hamiltonian are [34]

$$|\phi_k\rangle = \left[\frac{m\omega}{2^{2k}\pi\hbar(k!)^2}\right]^{1/4} H_k\left[\sqrt{\frac{m\omega}{\hbar}}\varphi\right] \exp\left[-\frac{m\omega\varphi^2}{2\hbar}\right], \tag{A.14}$$

where $k = 0, 1, 2, \ldots$ and where H_k are the Hermite polynomials.
We assume that a big-enough amount of these states (~ 30) can build a sufficient basis for the full

[1] This subsection is adapted from the calculations done by David López-Núñez

Hamiltonian's eigenstates. These eigenstates can thus be written as combination of the harmonic oscillator's eigenstates,

$$|\Psi\rangle = \sum_k c_k |\phi_k\rangle . \tag{A.15}$$

The harmonic oscillator is of course diagonal in its eigenbasis, and so the full Hamiltonian's elements can be expressed as

$$\begin{aligned}\mathcal{H}_{lk} &= \langle\phi_l| \mathcal{H} |\phi_k\rangle \\ &= k\hbar\omega\, \delta_{lk} - \frac{E_J}{2}\left[e^{-i2\pi f} \langle\phi_l| e^{i\varphi} |\phi_k\rangle + e^{i2\pi f} \langle\phi_l| e^{-i\varphi} |\phi_k\rangle\right],\end{aligned} \tag{A.16}$$

where δ_{lk} is Kronecker's delta.
The problem is now reduced to finding the matrix elements $\langle\phi_l| e^{\pm i\varphi} |\phi_k\rangle$. For that we use the expression [35]

$$\langle\phi_l| e^{c\hat{x}} |\phi_k\rangle = (k!\, l!)^{-1/2}\, e^{\frac{\hbar c^2}{4m\omega}} \sum_{j=0}^{min(k,l)} j! \binom{k}{j}\binom{l}{j}\left(\frac{\hbar}{2m\omega}\right)^{(k+l-2j)/2} c^{k+l-2j}. \tag{A.17}$$

In our case, $c = i$ and $\hat{x} = \hat{\varphi}$. Defining the variable $\theta = \sqrt{\frac{\hbar}{m\omega}} = \left(2\sqrt{\frac{2\beta_L E_C}{E_J}}\right)^{1/2}$, the expression ends in

$$\langle\phi_l| e^{i\varphi} |\phi_k\rangle = \frac{i^{k+l}\, e^{-\theta/4}}{\sqrt{2^{k+l}\, k!\, l!}} \sum_{j=0}^{min(k,l)} 2^j j! \binom{k}{j}\binom{l}{j}(-1)^j \theta^{l+k-2j}. \tag{A.18}$$

Parameter	Symbol	Value [units]
Critical Josephson junction current	I_c	0.65 [μA]
Josephson junction capacitance	C	20 [fF]
Self inductance	L	0.467 [nH]

Table A.1: rf-SQUID parameters used in simulation

B Coplanar Wave Guides

Coplanar waveguide (CPW) geometry is the most common way to define the superconducting circuit elements. In this method, the metallized elements, of width W, are placed on top of a dielectric substrate of height h and are surrounded by a ground plane, with a spacing S between them, where the substrate is exposed. A cross-section of a CPW geometry is shown in Fig. B.1.
CPW geometry is widely used in the field of microwave engineering [36], and as such has some analytic results we could use to estimate our sample's properties. These results were compared with Sonnet's numerical predictions and are found to be in a relatively good agreement.

B.1 Width and Spacing

In order to evaluate the characteristic impedance and effective permittivity of a CPW transmission-line, one can use the method of conformal mappings in order to get [37]:

$$\epsilon_e = 1 + \frac{\epsilon_r - 1}{2}\frac{K(k_1)}{K(k_1')}\frac{K(k_0')}{K(k_0)}, \tag{B.1}$$

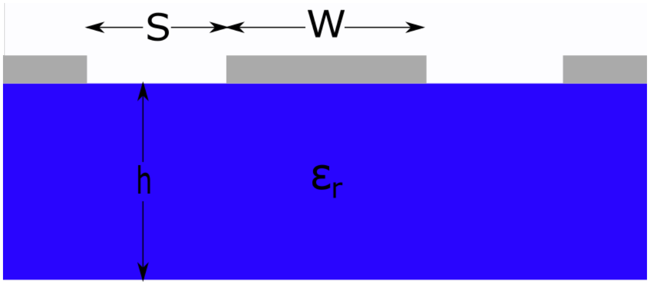

Figure B.1: Cross-section of a typical coplanar waveguide geometry. The metal (grey) is deposited on top of a substrate, with height h and dielectric constant ϵ_r. The width of the metallized line is W and its gap from the ground plane is S.

where

$$k_0 = \frac{W}{W + 2S} \qquad k_0' = \sqrt{1 - k_0^2} \tag{B.2}$$

$$k_1 = \frac{\sinh(\pi W/4h)}{\sinh\{[\pi(W + 2S)]/4h\}} \qquad k_1' = \sqrt{1 - k_1^2}. \tag{B.3}$$

Here, ϵ_r is the substrate's relative permittivity and $K(k)$ denotes the complete elliptic integral of the first kind with modulus k, which is a function of the coplanar resonator's width and spacing from the ground plane (W and S, respectively) and the dielectric substrate height (h).

Similarly, the characteristic impedance of a CPW can be calculated using the same method which gives,

$$Z_0 = \frac{30\pi}{\sqrt{\epsilon_e}} \frac{K(k_0')}{K(k_0)}. \tag{B.4}$$

These results show us that the characteristic impedance of the CPW line depends almost exclusively on its width-spacing ratio. We use this fact in order to keep this impedance constant throughout the chip. Fig. B.2a shows this result and the ratio chosen ($W = 2S$) in order to achieve an impedance of 50 Ω. The parameters used in this simulation are shown in table B.1.

Parameter	Symbol	Value [units]
Substrate's dielectric constant	ϵ_r	11.9
Substrate height	h	500 $[\mu m]$
CPW linewidth	W	1 $[\mu m]$

Table B.1: Coplanar waveguide parameters used in simulation

B.2 Transmission-Line Quarter-Wavelength Resonators

The resonators used in the chip are coplanar waveguide (CPW) transmission-line (TL) resonators, Where one end is shorted to the ground plane. We begin this section by looking into this kind of resonators and their properties, and finish it by taking a closer look at the specific resonators to be fabricated in our design.

In order to find the properties of a TL resonator, it is common to compare it to a conventional RLC-resonator. We use a result from Ref. [31] for the input impedance of a shorted line (not necessarily a resonator) of length l,

$$Z_{TL} = Z_0 \frac{1 - i \tanh \alpha l \cot \beta l}{\tanh \alpha l - i \cot \beta l}. \tag{B.5}$$

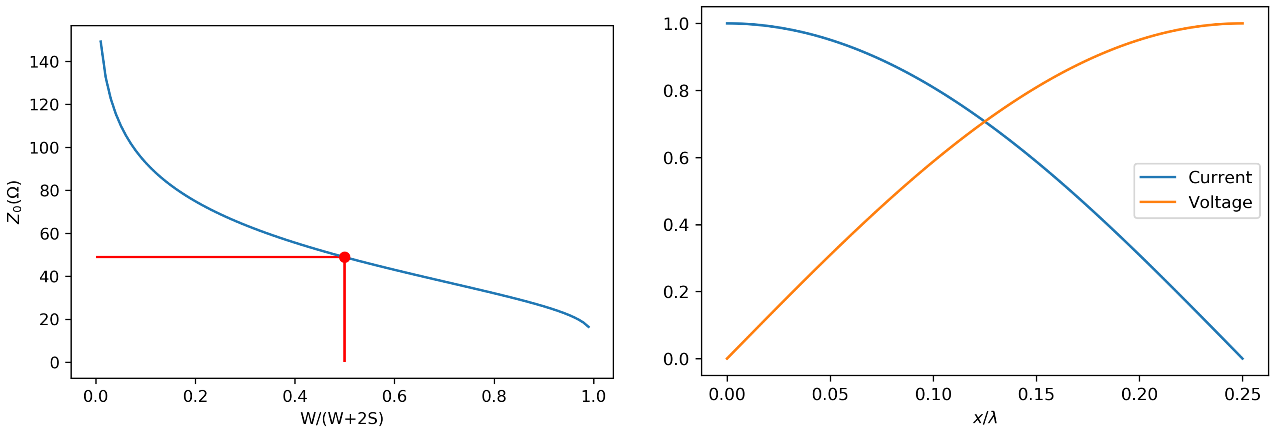

Figure B.2: (a) Characteristic impedance as a function of the ratio between a CPW linewidth (W) and the space between it and the ground plane (S), according to the conformal mapping analytic approximation. The chosen ratio, corresponding to $Z_0 = 50\ \Omega$ is highlighted. (b) Plot of current and voltage distribution along a $\frac{\lambda}{4}$-resonator. The TL resonator is shorted on one end (inductive coupling to feedline) and open on the other end (capacitive coupling to qubit), thus have (anti-)resonance with wavelengths equal four times its length. Only the first resonator mode is plotted.

Here Z_0 is the characteristic impedance (can be extracted using Eq. B.4), α is the attenuation constant and $\beta = \omega/v_p$ is the propagation constant in the line, where ω is the angular frequency of the propagating electromagnetic wave and $v_p = c/\sqrt{\epsilon_e}$ is its phase velocity.
Since the metal is superconducting at the temperatures we are considering and since the substrate on top of which it is evaporated has low tangent-loss ($\sim 4 \times 10^{-3}$) we can assume $\alpha l \ll 1$. We expect this resonator to be $\frac{\lambda}{4}$-resonator, and so we also make the change $l = \lambda/4$ for the resonator and so left with

$$Z_{TL} = iZ_0 \tan \frac{\beta\lambda}{4}. \tag{B.6}$$

We consider frequencies which are close to the resonance, $\omega = \omega_0 + \Delta\omega$, where $\omega_0 = 2\pi(v_p/\lambda)$, and get

$$\frac{\beta\lambda}{4} = \frac{\pi}{2} + \frac{\pi\Delta\omega}{2\omega_0} \tag{B.7}$$

and if $\Delta\omega \ll \omega_0$ we can make the approximation,

$$\tan \frac{\beta\lambda}{4} = \tan\left(\frac{\pi}{2} + \frac{\pi\Delta\omega}{2\omega_0}\right) = -\cot \frac{\pi\Delta\omega}{2\omega_0} \approx -\frac{2\omega_0}{\pi\Delta\omega}, \tag{B.8}$$

and so, finally,

$$Z_{TL} \approx -i\frac{Z_0}{\pi\Delta\omega/2\omega_0}. \tag{B.9}$$

This result should be compared to the general form of a parallel LC circuit,

$$Z_{LC} = -i\frac{\omega L}{\omega^2 LC - 1} \approx -i\frac{\omega L}{2[(\omega-\omega_0)/\omega_0]} \approx -i\frac{1}{2C(\omega-\omega_0)}, \tag{B.10}$$

where L is the circuit's inductance and C is its capacitance, and where the approximation is for frequencies close to the (anti-)resonance frequency $\omega_0 = 1/\sqrt{LC}$. One can see that the impedance is highest close to (anti-)resonance.

Comparing equations B.9 and B.10 gives

$$C_{TL} = \frac{\pi}{4\omega_0 Z_0} \tag{B.11}$$

$$L_{TL} = \frac{4Z_0}{\pi\omega_0}. \tag{B.12}$$

We can now use these values in order to estimate the resonator's *quality factor*. This is an important parameter in order have good control and readout of the qubit (see Sec. 4).
The quality factor of a resonator is defined as

$$Q = \omega\frac{E}{P} \tag{B.13}$$

where E is the average total energy stored in it and P is the energy dissipation rate. In general the total, or *loaded*, quality factor comprises the internal, or unloaded, quality factor and the external one, caused by the coupling of the resonator to other elements, e.g. feedline. Since the internal quality factor is very high with our choice of parameters, we choose its external quality factor to be approximately $5,000$, thus enabling us fast qubit readout while containing relatively small energy loss. Altogether we have [31]

$$Q_L^{-1} = Q_i^{-1} + Q_e^{-1} \approx Q_e^{-1}. \tag{B.14}$$

The (magnetic) energy stored in the resonator's inductor is

$$W_L = \frac{1}{4}\left|I_L\right|^2 L_{TL}, \tag{B.15}$$

where I_L is the current through the inductor, and since at resonance it equals the average energy stored in the capacitor we have

$$E = \frac{1}{2}\left|I_L\right|^2 L_{TL}. \tag{B.16}$$

The loss due to a loaded impedance Z_L is

$$P = \frac{1}{2}Z_{TL}\left|I\right|^2 = 2Z_{TL}\left|I_L\right|^2, \tag{B.17}$$

and so

$$Q_L = \frac{\omega L_{TL}}{4Z_{TL}}. \tag{B.18}$$

B.2.1 Resonators in our Design

Our transmission-line $\frac{\lambda}{4}$-resonator is made of three parts, namely its coupler to the feedline, its meanders and its coupler to the qubit. A schematic of this design, albeit with fewer meanders, is shown in Fig. B.3.
The total length of the resonator is

$$l = \underbrace{\frac{E}{2} + r\frac{\pi}{2}}_{\text{Feedline coupler}} + \underbrace{2n(E + r\pi)}_{\text{n Meanders}} + \underbrace{\frac{E}{2} + r\left(\pi - 1\right)}_{\text{Qubit coupler}},$$

where E is the elongation, n is the meanders number and r is the radius of a meander and is equal to 5 times the linewidth (a useful minimum to avoid uncontrolled field lines). Notice that this equation holds only for the specific resonator design used for this chip. A schematic drawing the resonator used can be seen in figure B.3.
We can then calculate its bare resonance frequency:

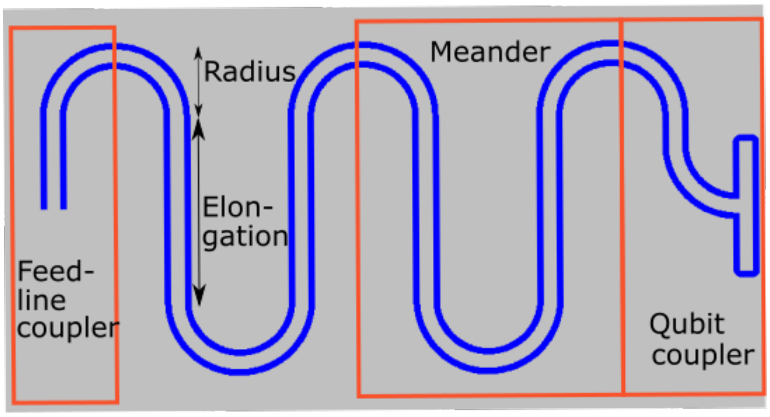

Figure B.3: $\frac{\lambda}{4}$-resonator with its parts,characteristic lengths and its surrounding ground plane. All three parts of the resonator (two meanders in this design) are clearly indicated by the rectangles. The evaporated aluminum is in grey and the exposed silicon substrate is in blue.

$$\frac{\omega_0}{2\pi} = \frac{v_p}{\lambda} = \frac{c}{\sqrt{\epsilon_e}} \frac{1}{4l}$$

where v_p is the phase velocity, c is the speed of light in vacuum and ϵ_e is the relative effective dielectric permittivity and is calculated using, e.g. Eq. B.1.
Together we can calculate the necessary resonator elongation to achieve a specific resonance frequency:

$$E(n,r) = \frac{(c/4f\sqrt{\epsilon_e}) - r(\pi/2-1)}{2n+1} - \pi r$$

where we explicitly mark its dependence on n and r since they are parameters of the resonator and not its environment.

This equation is used in the Python code we created in order to draw a file which will be later read by the lithography machines.

C Lab Characterization

In Sec. 3 we discussed noise and its effect on the qubit's life-times. Before installing the equipment in the new lab we therefore ran some measurements in order to make sure that the environmental noise is reduced to a minimum.
We focused on three noise sources: mechanical vibrations, electromagnetic fields and radiation. Mechanical vibrations and electromagnetic fields can cause flux and charge fluctuations, and are therefore mitigated by shielding the fridge and and adding shock absorbers beneath it.
An example of a magnetic field measurement is shown in Fig. C.1. In order to understand the source of this noise we perform a Power Spectral Density (PSD) analysis and find that the main source is at 50 Hz and 150 Hz, as expected from fields coming from standard home electricity network. Both peaks are within the range of amplitudes we expect ($< 40\ dB$).

Radiation effects (both radioactive and cosmic) were shown recently to have an effect on qubit's coherence, by breaking Cooper-pairs into quasi-particles [38, 39]. The radiation effects, however, is not very relevant for today's qubits, since their characteristic decay times are usually one order of magnitude *longer* than that of the qubits. Despite that, we measured the radiation in the lab and found it to be normal ($< 0.25\ \mu Sv/h$).

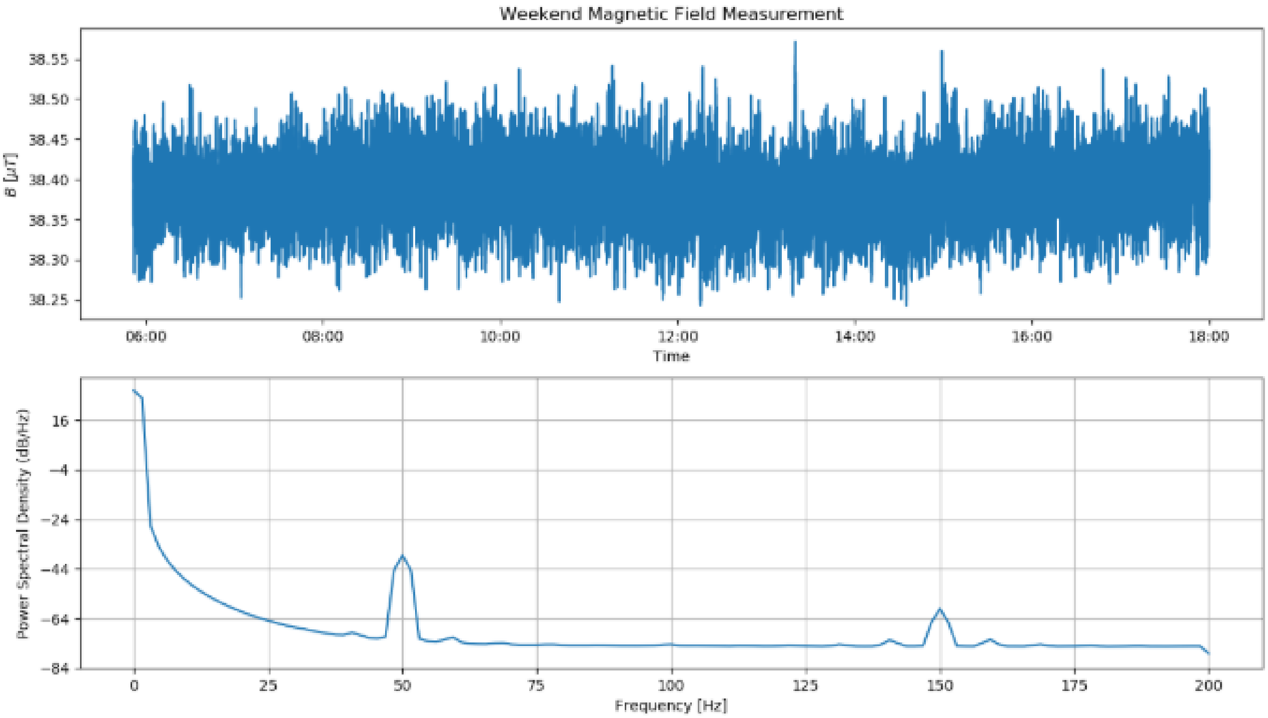

Figure C.1: Magnetic field measurement in the lab. In the top panel the raw data of a long measurement (over a weekend) is shown, and its PSD analysis is given in the bottom panel. Notice the two peaks, corresponding to home electricity network frequencies.